Radial orbital anisotropy and the Fundamental Plane of elliptical galaxies

C. Nipoti,[1] P. Londrillo[2] and L. Ciotti[2,3,4]★

[1]*Dipartimento di Astronomia dell'Università degli Studi di Bologna, via Ranzani 1, 40127 Bologna, Italy*
[2]*Osservatorio Astronomico di Bologna, via Ranzani 1, 40127 Bologna, Italy*
[3]*Scuola Normale Superiore, Piazza dei Cavalieri 7, 56126 Pisa, Italy*
[4]*Department of Astrophysical Sciences, Princeton University Observatory, Ivy Lane, NJ 08544, USA*

ABSTRACT

The existence of the Fundamental Plane imposes strong constraints on the structure and dynamics of elliptical galaxies, and thus contains important information on the processes of their formation and evolution. Here we focus on the relations between the Fundamental Plane thinness and tilt and the amount of radial orbital anisotropy: in fact, the problem of the compatibility between the observed thinness of the Fundamental Plane and the wide spread of orbital anisotropy admitted by galaxy models has often been raised. By using N-body simulations of galaxy models characterized by observationally motivated density profiles, and also allowing for the presence of live, massive dark matter haloes, we explore the impact of radial orbital anisotropy and instability on the Fundamental Plane properties. The numerical results confirm a previous semi-analytical finding (based on a different class of one-component galaxy models): the requirement of stability matches almost exactly the thinness of the Fundamental Plane. In other words, galaxy models that are radially anisotropic enough to be found outside the observed Fundamental Plane (with their isotropic parent models lying on the Fundamental Plane) are unstable, and their end-products fall back on the Fundamental Plane itself. We also find that a systematic increase of radial orbit anisotropy with galaxy luminosity cannot explain by itself the whole tilt of the Fundamental Plane, the galaxy models becoming unstable at moderately high luminosities: at variance with the previous case, their end-products are found well outside the Fundamental Plane itself. Some physical implications of these findings are discussed in detail.

Key words: galaxies: elliptical and lenticular, cD – galaxies: evolution – galaxies: formation – galaxies: kinematics and dynamics.

1 INTRODUCTION

The Fundamental Plane (FP) of elliptical galaxies (Djorgovsky & Davies 1987; Dressler et al. 1987) is a scaling relation between three of their basic *observational* properties, namely the circularized effective radius $\langle R \rangle_e \equiv \sqrt{a_e b_e}$ (where a_e and b_e are the major and minor semi-axis of the effective isophotal ellipse), the central velocity dispersion σ_0, and the mean effective surface brightness $\langle I \rangle_e \equiv L_B/2\pi\langle R \rangle_e^2$ (where L_B is the luminosity of the galaxy, for example in the Johnson B band). An interesting parametrization of the FP, which we adopt in this paper, has been introduced by Bender, Burstein & Faber (1992, hereafter BBF):

$$k_1 \equiv \frac{\log \sigma_0^2 + \log\langle R \rangle_e}{\sqrt{2}}, \tag{1}$$

$$k_2 \equiv \frac{\log \sigma_0^2 + 2\log\langle I \rangle_e - \log\langle R \rangle_e}{\sqrt{6}}, \tag{2}$$

$$k_3 \equiv \frac{\log \sigma_0^2 - \log\langle I \rangle_e - \log\langle R \rangle_e}{\sqrt{3}}. \tag{3}$$

In particular, when projected on the (k_1, k_3) plane, the FP is seen almost edge-on and it is considerably thin, while the distribution of galaxies in the (k_1, k_2) plane is considerably broader. For example, Virgo ellipticals studied by BBF are distributed on the (k_1, k_3) plane according to the best-fitting relation

$$k_3 = 0.15k_1 + 0.36 \tag{4}$$

(when adopting respectively, kpc, km s^{-1} and $L_{B\odot}$ pc^{-2} as length, velocity and surface brightness units), with a very small dispersion of $\sigma(k_3) \simeq 0.05$ over all the range spanned by the data, $2.6 \lesssim k_1 \lesssim 4.6$ (and so $0.75 \lesssim k_3 \lesssim 1.05$, see e.g. Ciotti, Lanzoni & Renzini 1996, hereafter CLR96).

★E-mail: ciotti@bo.astro.it

By combining equations (1) and (3) with equation (4) the FP equation of BBF is then obtained directly in terms of the observables: the exponents are in good agreement with those derived (in the Johnson B band) from a much larger galaxy sample by Jørgensen, Franx & Kjærgaard (1996).

Note that equation (4) implies that for galaxies of given luminosity L_B their effective radius and central velocity dispersion must be strongly coupled: in fact at any fixed luminosity the coordinates k_3 and k_1 are related through definitions (1) and (3) by

$$k_3 = \sqrt{\frac{2}{3}}k_1 + \sqrt{\frac{1}{3}}\log\frac{2\pi}{L_B}, \qquad (5)$$

and the slope of this relation ($\simeq 0.82$) is different from that of the FP ($\simeq 0.15$). As a consequence, in the (k_1, k_3) plane all galaxies with the same luminosity are located on straight lines significantly inclined with respect to the FP: the presence of substantial scatter in galactic properties from galaxy to galaxy (of similar luminosity) would destroy the thinness of the FP by producing a large scatter in k_1 and so in k_3.

The relation between galaxy properties and the FP can be expressed in a quantitative way under the reasonable assumption that present-day ellipticals are virialized systems. We write the virial theorem as

$$\frac{GL_B\Upsilon_*}{\langle R\rangle_e} = K_V\sigma_0^2, \qquad (6)$$

where $\Upsilon_* = M_*/L_B$ is the galaxy *stellar* mass-to-light ratio (for example in Blue solar units), and K_V is a dimensionless factor depending on the stellar density profile, internal dynamics, dark matter amount and distribution and, for non-spherical galaxies, on their relative orientation with respect to the observer's line of sight (see e.g. Ciotti 1997); in addition, K_V depends also on the observing aperture adopted to derive σ_0.

Equations (4) and (6) imply that, for galaxies belonging to the FP, the quantity Υ_*/K_V is a very well defined function of two[1] of the three observables L_B, σ_0 and $\langle R\rangle_e$. In the particular case of adopting the numerical coefficients of equation (4), measuring L_B in $10^{10} L_{B\odot}$, and taking into account that $k_1 = \log(G\Upsilon_* L_B/K_V)/\sqrt{2}$ and $k_3 = \log(2\pi G\Upsilon_*/K_V)/\sqrt{3}$,

$$\frac{\Upsilon_*}{K_V} \simeq 1.12 \times L_B^{0.23}, \qquad (7)$$

where the quantity Υ_*/K_V is characterized by a scatter of $\simeq 20$ per cent owing to its relation with k_3 (however, additional considerations reduce this figure to $\simeq 12$ per cent, see Renzini & Ciotti 1993). As a consequence, any departure from the relation dictated by equation (7) will move a galaxy away from the FP. We recall here that the dependence of k_3 on k_1, as given by equation (4) and responsible for the luminosity dependence of the ratio Υ_*/K_V, is commonly known as the FP 'tilt'.

The simple analysis presented above shows that the two properties of thinness and tilt of the FP are deeply connected with the present-day structure and dynamics of ellipticals (hereafter, Es), and, as a consequence, with their formation and evolution history: the very existence of the FP [as well as of the other tight

scaling relations revealing the remarkable homogeneity of Es, such as the $M_{BH}-\sigma_0$ (Ferrarese & Merritt 2000; Gebhardt et al. 2000), the $Mg_2-\sigma_0$ (Bender, Burstein & Faber 1993 and references therein) and the colour–magnitude (Bower, Lucey & Ellis 1992) relations] imposes strong constraints on the different formation and evolutionary scenarios proposed for Es (i.e. dissipationless merging, monolithic collapse or a combination of the two; see e.g. Ciotti & van Albada 2001).

Among the various galaxy properties in principle able to destroy the FP thinness (as a consequence of a substantial variation at fixed galaxy luminosity), one of the most 'effective' is certainly orbital anisotropy (de Zeeuw & Franx 1991). In fact, galaxy models are commonly believed to be able to sustain a large spread of orbital anisotropies and it is also well known that radial orbital anisotropy can produce very high *central* velocity dispersion values, and correspondingly low values of K_V, thus substantially violating equation (7). A natural question to be addressed is then what physical principle or evolutionary process limits the range of orbital anisotropies shown by real galaxies. Ciotti & Lanzoni (1997, hereafter CL97), using one-component, radially anisotropic Sersic (1968) models, and a semi-analytical investigation based on the Fridman & Polyachenko (1984, hereafter FP84) stability indicator, suggested the possibility that radial orbit instability could be the limiting factor of the FP thickness. In practice, CL97 found indications that galaxy models sufficiently anisotropic to be outside the FP observed thickness (when their parent isotropic model was assumed to lie on the FP) were unstable. Clearly, this preliminary indication requires a confirmation with the aid of numerical simulations and more realistic galaxy models (for example, allowing for the presence of live dark matter haloes). Also, a question naturally associated with that above is the determination of the position of the end-products of unstable initial conditions in the space of the observables. One of the aims of this work is indeed to answer these two questions by numerical simulations of one- and two-component radially anisotropic galaxy models.

Orbital anisotropy is not only related to the problem of the FP thinness but also one of the candidates that has been proposed to explain the origin of the FP tilt (CLR96; CL97). If this were the case, the amount of radial anisotropy in the velocity dispersion tensor should increase with galaxy luminosity, as can be seen from equation (7) under the assumption of a constant Υ_* and of structural homology[2] over the whole FP plane. In other words, in this scenario the FP tilt would be produced by a *dynamical* non-homology arising from anisotropy (note that dynamical non-homology may well coexist with structural homology, but the converse is in general not true). Many interesting questions are raised by the scenario depicted above: for example, under the assumption that an isotropic galaxy of given luminosity lies on the FP, how far can the derived structurally homologous but radially anisotropic models climb over the FP before the onset of radial orbit instability? In addition, what happens to the end-products of the unstable models? Will they remain near the FP? In this paper we try to address also these questions with the aid of N-body numerical simulations.

Strictly related to the clarification of the interplay between orbital anisotropy and the FP tilt, is the possibility to obtain some clues on the formation processes of Es. In fact it is trivial to prove that, as consequence of the virial theorem and the conservation of

---

[1] In principle one could find virialized galaxies *everywhere* in the three-dimensional observational $(L_B, \sigma_0, \langle R\rangle_e)$ space. From this point of view the existence of the FP is related to the virial theorem as the HR diagram is related to hydrostatic equilibrium: the useful information that one derives is *not* about the equilibrium equations, but the physics of the objects involved.

[2] With 'structural homology' we mean that all the structural galaxy properties (e.g. the stellar and dark halo density profiles, the ratio of their scalelengths and masses, and so on) *do not depend* on L_B.

the total energy, in the merging of two galaxies with masses M_1 and M_2 and virial velocity dispersions $\sigma_{v,1}$ and $\sigma_{v,2}$, the virial velocity dispersion of the resulting galaxy is given by

$$\sigma_{v,1+2}^2 = \frac{M_1\sigma_{v,1}^2 + M_2\sigma_{v,2}^2}{M_1 + M_2} \tag{8}$$

(by definition $\sigma_v^2 \equiv 2T/M$, where T is the total kinetic energy of the galaxy). For simplicity in the formula above we considered, in the initial conditions, a negligible energy of the galaxy pair when compared with the other energies involved in the process, and no significant mass loss from the resulting system. From equation (8) it follows that $\sigma_{v,1+2} \leq \max(\sigma_{v,1}, \sigma_{v,2})$, i.e. the *virial* velocity dispersion cannot increase in a merging process of the kind described above. On the other hand, the FP (or the less tight Faber–Jackson relation; Faber & Jackson 1976) indicates that the *projected, central* velocity dispersion increases with galaxy luminosity. Then, in the dissipationless merging scenario the FP tilt can be produced only by structural and/or dynamical non-homology, since the relation between central and virial velocity dispersion depends on the structure and dynamics of the system: in particular we will discuss here the second possibility, with regard to an increase in radial orbital anisotropy with galaxy luminosity. Note that an increase in the radial orbit amount has been claimed in the past as a natural by-product of galaxy merging, and also some observations have been interpreted in this way (Bender 1988; see also Naab, Burkert & Hernquist 1999, and references therein). With the aid of the explored numerical models we will try to obtain some qualitative insight into this problem: it is however clear that the results should be considered at the best qualitative indications, and that a firm answer about the role of merging in producing the FP tilt can be obtained only with N-body numerical simulations of merging galaxies (see e.g. Capelato, de Carvalho & Carlberg 1995).

Summarizing, the aims of this work are the following. Concerning the FP thickness problem, we investigate the role of radial orbit instability as a factor regulating the amount of radial anisotropy for galaxies of given luminosity, and the position, relative to the FP, of the end-products of radially unstable anisotropic models. In addition, we determine whether it is possible to reproduce the whole FP tilt with a systematic variation of radial anisotropy with luminosity (using both stable and unstable initial conditions), and the fate of unstable models initially forced to lie on the FP. This paper is organized as follows. In Section 2 we describe the basic structural and dynamical properties of the investigated models; a short description of the codes used for the numerical simulations is also given. In Section 3 we present the results and their impact on the FP thinness problem, and in Section 4 the results are discussed focusing on the origin of the FP tilt. Finally, in Section 5 the main conclusions are summarized.

2 MODELS

2.1 Initial conditions

2.1.1 Structural and dynamical properties

As initial conditions for the N-body simulations we use spherically symmetric one-component γ models (Dehnen 1993; Tremaine et al. 1994) and two-component (γ_1, γ_2) models (Ciotti 1996, 1999). The density, mass, and (relative) potential profiles of the stellar component are given by

$$\rho_*(r) = \frac{3-\gamma}{4\pi}\frac{M_*r_c}{r^\gamma(r_c+r)^{4-\gamma}} \qquad (0 \leq \gamma < 3), \tag{9}$$

$$\frac{M_*(r)}{M_*} = \left(\frac{r}{r_c+r}\right)^{3-\gamma}, \tag{10}$$

$$\Psi_*(r) = \frac{GM_*}{r_c(2-\gamma)}\left[1 - \left(\frac{r}{r_c+r}\right)^{2-\gamma}\right] \quad (\gamma \neq 2), \tag{11}$$

$$\Psi_*(r) = \frac{GM_*}{r_c}\ln\frac{r_c+r}{r} \qquad (\gamma = 2), \tag{12}$$

where M_* is the total stellar mass; the $\gamma = 1$ and $\gamma = 2$ cases correspond to Hernquist (1990) and Jaffe (1983) density distributions, two reasonable approximations (when projected) of the $R^{1/4}$ law (de Vaucouleur 1948). In the two-component models, the dark matter (DM) halo is described by ρ_h, M_h and Ψ_h profiles of the same family of equations (9)–(12), where now $r_h \equiv \beta r_c$ and $M_h \equiv \mu M_*$.

Radial anisotropy in the stellar orbital distribution is introduced by using the Osipkov–Merritt (OM) parametrization (Osipkov 1979; Merritt 1985). The distribution function (DF) of the stellar component is then given by

$$f_*(Q) = \frac{1}{\sqrt{8}\pi^2}\frac{\mathrm{d}}{\mathrm{d}Q}\int_0^Q \frac{\mathrm{d}\varrho_*}{\mathrm{d}\Psi_T}\frac{\mathrm{d}\Psi_T}{\sqrt{Q-\Psi_T}}, \tag{13}$$

where

$$\varrho_*(r) = \left(1 + \frac{r^2}{r_a^2}\right)\rho_*(r). \tag{14}$$

The variable Q is defined as $Q \equiv \mathcal{E} - L^2/2r_a^2$, where the relative (positive) energy is given by $\mathcal{E} = \Psi_T - v^2/2$, v is the modulus of the velocity vector, the relative total potential is $\Psi_T = \Psi_* + \Psi_h$, L is the angular momentum modulus per unit mass, and $f_*(Q) = 0$ for $Q \leq 0$. The quantity r_a is the so-called 'anisotropy radius': for $r \gg r_a$ the velocity dispersion tensor is mainly radially anisotropic, while for $r \ll r_a$ the tensor is nearly isotropic. Isotropy is realized at the model centre, independently of the value of r_a; in the limit $r_a \to \infty$, $Q = \mathcal{E}$ and the velocity dispersion tensor becomes globally isotropic.

In order to reduce the dimensionality of the parameter space, the orbital distribution of the DM haloes is assumed isotropic in all our simulations; as a consequence the DF for the DM halo component, $f_h(\mathcal{E})$, is given by equation (13) where $Q = \mathcal{E}$ and $\rho_h(r)$ substitutes $\varrho_*(r)$.

2.1.2 Physical scales

According to the given definitions, from the structural and dynamical point of view the one-component models are completely determined by four quantities: the two physical scales M_* and r_c and the two dimensionless parameters γ and $s_a \equiv r_a/r_c$.

In the numerical simulations M_*, r_c and T_{dyn} are adopted as mass-, length- and time-scales. T_{dyn} is the half-mass dynamical time, defined as

$$T_{dyn} \equiv \sqrt{\frac{3\pi}{16G\rho_M}} = \pi\sqrt{\frac{r_c^3}{2GM_*}}F(\gamma), \tag{15}$$

where $\rho_M = 3M_*/8\pi r_M^3$ is the mean density inside the half-mass radius r_M and

$$F(\gamma) = \left(2^{\frac{1}{3-\gamma}} - 1\right)^{-\frac{3}{2}}. \tag{16}$$

Note that at fixed M_* and r_c the half-mass dynamical time depends

strongly on γ. For example, $F(0)/F(1) \simeq 2.0$ and $F(1)/F(2) \simeq 3.8$. Finally, the velocity scale is given by

$$v_{\rm c} \equiv \frac{r_{\rm c}}{T_{\rm dyn}} = \frac{1}{\pi F(\gamma)} \sqrt{\frac{2GM_*}{r_{\rm c}}}. \qquad (17)$$

In the case of two-component galaxies we limit our present study to (1,1) models, i.e. to two-component Hernquist models (Ciotti 1996). In this way the DM halo is similar to Navarro, Frenk & White (1996) profiles. (1,1) models are characterized by five quantities, the two physical scales M_* and $r_{\rm c}$ and the three dimensionless parameters $s_{\rm a}$, μ and β. Their $T_{\rm dyn}$ depends on μ and β: from definition (15), where now $\rho_{\rm M} = 3(1 + \mu)M_*/(8\pi r_{\rm M}^3)$ and $r_{\rm M}$ is the half-mass radius of the total (stellar plus dark) density distribution, it results that

$$T_{\rm dyn} = \pi \sqrt{\frac{r_{\rm c}^3}{2GM_*}} F(\mu, \beta), \qquad (18)$$

where $F = x^{3/2}(\mu, \beta)/\sqrt{1 + \mu}$, and x is the solution of

$$\left(\frac{x}{1 + x}\right)^2 + \mu \left(\frac{x}{\beta + x}\right)^2 = \frac{1 + \mu}{2}. \qquad (19)$$

Finally note that, once the dimensionless numbers $s_{\rm a}$ and γ (for one-component models) and $s_{\rm a}$, μ and β (for two-component models) are fixed, the results of the numerical simulations can be rescaled for arbitrary values of M_*, $r_{\rm c}$ and $L_{\rm B}$ (or Υ_*). In particular, in order to transform the results of the numerical simulations in physical units we express M_* in $10^{10} {\rm M}_\odot$, $r_{\rm c}$ in kpc and $L_{\rm B}$ in $10^{10} L_{\rm B\odot}$.

2.1.3 Numerical realization of the initial conditions

In order to arrange the initial conditions for the numerical simulations, we distribute N particles ($N = 32\,768$ and $N = 131\,072$ for one- and two-component models, respectively) by using spherical coordinates (r, ϑ, φ for positions, and $v_{\rm r}, v_\vartheta, v_\varphi$ for velocities). The radial coordinate is assigned by inverting equation (10) and choosing a sampling suited to resolve the core of the distribution, while angular coordinates are given randomly. The velocity vector of each particle is assigned by using the von Neumann rejection method. This method can be easily applied to OM systems by introducing the dimensionless vector of components (u_1, u_2, u_3), related to ($v_{\rm r}, v_\vartheta, v_\varphi$) by

$$v_{\rm r} = \sqrt{2\Psi_{\rm T}} u_1, \quad v_\vartheta = \frac{\sqrt{2\Psi_{\rm T}}}{\nu_{\rm a}} u_2, \quad v_\varphi = \frac{\sqrt{2\Psi_{\rm T}}}{\nu_{\rm a}} u_3, \qquad (20)$$

where

$$\nu_{\rm a} = \sqrt{1 + \frac{r^2}{r_{\rm a}^2}}; \qquad (21)$$

from this choice $0 \le u \le 1$, where $u = \sqrt{u_1^2 + u_2^2 + u_3^2}$. The vector ($u_1, u_2, u_3$) is assigned to each particle by using the rejection method, after computing the value of the DF at the required $Q = (1 - u^2)\Psi_{\rm T}$, by numerically evaluating equation (13). The components of the velocity vector ($v_{\rm r}, v_\vartheta, v_\varphi$) are then recovered according to equation (20). The initial conditions so obtained are then compared to the expected analytical density distribution, finding, as a rule, an agreement of better than 2 per cent over the radial interval containing 0.99 of the total mass of the theoretical model.

2.2 The numerical codes

For our simulations we used the Barnes & Hut (1986) TREECODE (in a version made publicly available by Hernquist 1987) and the Springel, Yoshida & White (2000) parallel version of GADGET (adapted to run on the 32-processor Cray T3E at CINECA). In particular, the one-component simulations were run on a Alpha workstation by using the TREECODE with $N = 32\,768$; for some of them we used also $N = 65\,536$. The quadrupole correction in the cell–particle force calculation was always applied. For the two-component models we used instead GADGET with $N = 131\,072$; in addition, some one-component models were also tested with $N = 131\,072$ using the same code. We found very good agreement between the test simulations performed with both the codes, with the basic properties of the simulated systems nearly independent of the adopted number of particles.

From the numerical point of view, TREECODE simulations are characterized by three parameters, namely the opening angle θ, the softening parameter ε (i.e. the softening length expressed in units of $r_{\rm c}$) and the time-step Δt. Following Hernquist (1987) and Barnes & Hut (1989), we assume $\theta = 0.8$, a good compromise between conservation of total energy and computational time. The choice of Δt and ε requires some care; in fact these two parameters are strongly coupled and, in order to maintain the same accuracy in the force evaluation, Δt must be reduced if ε is reduced (Barnes & Hut 1989). In addition, the 'optimal' value of the softening length is strongly dependent on N and on the specific density distribution profile (Merritt 1996; Athanassoula et al. 2000; Dehnen 2001). To choose the values of these parameters, we performed some simulations of isotropic γ models over $100\, T_{\rm dyn}$, checking the total energy E and virial ratio ($V = 2T/W$) conservation. On the basis of these tests we adopt $\Delta t = T_{\rm dyn}/100$, and $\varepsilon = (0.072, 0.030, 0.016)$ for $\gamma = (0, 1, 2)$ models, respectively. With this choice we obtain $|\Delta E/E| < 1.5$ per cent and $|\Delta V/V| < 2$ per cent. GADGET simulations depend on five parameters: the cell-opening parameter α, the minimum and the maximum time step $\Delta t_{\rm min}$ and $\Delta t_{\rm max}$, the time-step tolerance parameter $\alpha_{\rm tol}$, and the softening parameter ε (Springel et al. 2000). Fiducial values of the parameters were fixed after running a few one-component ($\gamma = 1$) test simulations. In particular, with $\alpha = 0.02$, $\Delta t_{\rm min} = 0$, $\Delta t_{\rm max} = T_{\rm dyn}/100$, $\alpha_{\rm tol} = 0.05$, and $\varepsilon = 0.016$ we obtain $|\Delta E/E| < 0.5$ per cent and $|\Delta V/V| < 1$ per cent. The value of the first four parameters were also used in the two-component simulations. The softening length ε was instead determined case by case, by considering the core radius length of the more concentrated component.

In order to determine the 'observational' properties of the end-products of the numerical simulations, and place them in the (k_1, k_2, k_3) space, we measured their effective radius $\langle R \rangle_{\rm e}$, central velocity dispersion σ_0 and mean effective surface brightness $\langle I \rangle_{\rm e}$ for several projection angles. The technical details of the adopted procedures are given in the Appendix, together with a brief discussion on the discreteness effects on the derived values of the 'observational' properties of the models. A point of interest is the choice of the adopted 'aperture radius' for the measure of σ_0, fixed in this work to $\langle R \rangle_{\rm e}/8$ in order to match the observational procedure at low redshifts (see, e.g., Jørgensen et al. 1996). Indeed, it is well known that isotropic γ-models may present a projected velocity dispersion profile decreasing toward the centre (in contrast to what happens in the vast majority of elliptical galaxies): for example, the projected velocity dispersion of Hernquist models peaks approximately at $R_{\rm e}/5$, while the profile for (isotropic) Jaffe models is monotonically decreasing. As a consequence, the

position of the initial conditions and of the end-products in the k space could depend on the adopted aperture radius used to measure σ_0. In order to assess the effect of this choice on our conclusions, we analysed the results of the simulations also by using an aperture radius of $\langle R \rangle_e / 4$, and we found very good agreement with the results obtained with the aperture $\langle R \rangle_e / 8$: therefore, we present here only these last results. Note however that, by virtue of the projected virial theorem (see e.g. Ciotti 1994), a totally different scenario from that explored in this paper would arise in the limiting case of σ_0 measured over the whole galaxy: anisotropy would play no role at all in determining the position of initial conditions in the k space, and any difference between initial and final σ_0 would be only caused by projection effects associated with loss of spherical symmetry. These aperture effects could be important when studying the FP observationally at intermediate redshift (see e.g. van Dokkum & Franx 1996; Bender et al. 1998; Pahre, Djorgovski & de Carvalho 1998; Treu et al. 1999), or locally by using large apertures (see e.g. Graham & Colless 1997).

3 ORBITAL ANISOTROPY AND THE FP THINNESS

As already pointed out in the Introduction, the 1σ dispersion of the observational data around the best-fitting relation (4) is surprisingly small and nearly constant over all the observed range in k_1, with $\sigma(k_3) \simeq 0.05$. We investigate here the constraints imposed by this tightness on the amount of radial orbital anisotropy for the set of one- and two-component galaxy models described in Section 2. We start by fixing the values for the dimensionless parameters γ (for one-component models) and μ and β (for two-component models); we also assume global isotropy, i.e., $s_a \to \infty$, and in this way the quantity K_V is uniquely determined. These globally isotropic models (which we call *parent models*) are then placed on the FP by assigning of the pair (Y_*, L_B) so that equation (7) is verified. From each of these parent models lying on the FP we then generate a *family* of OM radially anisotropic models by decreasing s_a, while maintaining all the other model parameters fixed. Correspondingly K_V decreases (as can be seen from Table 1, in the case of one-component models and for representative values of the parameter s_a), k_1 increases, and so does k_3, according to equation (5): for sufficiently small values of s_a the members of each family are found outside the observed thickness of the FP. Note that by an appropriate choice of the pair (Y_*, L_B) each parent isotropic model can be placed at arbitrary positions over the best-fitting line (4), and so the results of the numerical simulations (after a rescaling to Y_* and L_B) are the same everywhere on the FP. In addition, since $\sigma(k_3)$ is constant over the whole observational range spanned by k_1, the conclusions obtained from each family of models are also independent of the position of the parent galaxy on the FP. Obviously all isotropic models discussed in this paper are stable (see e.g. Binney & Tremaine 1987; Ciotti 1996), while for each family of models a critical value s_{as} for *stability* exists such that the initial conditions characterized by $s_a < s_{as}$ describe radially unstable configurations. From the point of view of the present discussion, the critical value s_{as} corresponds, through $K_V(s_{as})$, to the maximum distance that a *stable* model can have from the FP, where its parent isotropic model lies at (say) (k_1^{iso}, k_3^{iso}). Clearly, initial conditions describing unstable models can be placed at larger distances from the FP: these initial conditions will evolve with time, and their representative points in the space of observables will also evolve with time, up to virialization. In particular,

Table 1. The dimensionless coefficient $K_V(\gamma, s_a)$ for one-component models, as obtained from equation (6). See Section 3 for the definitions of s_{ac} and s_{as}.

γ	$K_V(\gamma, \infty)$	$K_V(\gamma, s_{as})$	$K_V(\gamma, s_{ac})$
0	6.7	5.9	2.8
1	5.9	5.3	2.7
2	4.8	4.4	2.3

the coordinates $k_1(t)$ and $k_3(t)$ will evolve with time moving on the line described by equation (5). Note that the maximum distance from the FP at which unstable models can be placed is in general finite: in fact, the anisotropy radius of all physically acceptable (stable and unstable) galaxy models must satisfy the inequality $s_a \geq s_{ac}$, where $s_{ac} \leq s_{as}$ is the (dimensionless) critical anisotropy radius for *consistency* (i.e., the anisotropy limit for initial states with a nowhere negative DF); for a study of s_{ac} in γ models and in (γ_1, γ_2) models see Carollo, de Zeeuw & van der Marel (1995) and Ciotti (1996, 1999).

FP84 argued that a quantitative indication of the maximum amount of radial orbits sustainable by a specific density profile is given by the stability parameter $\xi = 2T_r/T_t$, where T_r and $T_t \equiv T_\vartheta + T_\varphi$ are the radial and tangential component of the kinetic energy tensor, respectively. From its definition $\xi \to 1$ for $s_a \to \infty$ (globally isotropic models), while $\xi \to \infty$ for $s_a \to 0$ (fully radially anisotropic models). The fiducial value indicated by FP84 as a boundary between stable and radially unstable systems is $\xi_s \simeq 1.7$. Unfortunately, the reliability of such an indicator is not well understood, and indications exist of a significant dependence on the particular density profile under scrutiny (see e.g. Merritt & Aguilar 1985; Bertin & Stiavelli 1989; Saha 1991, 1992; Bertin et al. 1994; Meza & Zamorano 1997). In any case, CL97 used this value to determine s_{as} for one-component Sersic (1968) models by solving the associated Jeans equations, and from this value they determined the maximum distance of stable models from the FP: all models characterized by $\xi < \xi_s$ were found inside the observed thickness of the FP. This finding can be considered at the best a qualitative indication, considering the uncertainties associated with the exact value of ξ_s and its dependence on the specific density profile adopted, and the need of numerical simulations is clear.

With the aid of N-body simulations in the following two sections we investigate how distant from the FP stable models of various families can be placed, by increasing their radial orbital anisotropy. The logically related question of what happens to the end-products of the unstable (but physically consistent) initial conditions is also addressed.

Owing to its central role in the following discussion, it is important to quantify the concept of 'distance' of a galaxy model from the FP. In general, we define the distance of a point (k_1, k_3) from the FP as the quantity $\delta k_3 \equiv |k_3 - 0.15 k_1 - 0.36|$, i.e. the distance at fixed k_1 between the point and the FP itself: this quantity naturally is comparable with $\sigma(k_3)$. Unfortunately, as already discussed in the Introduction, galaxy models of fixed luminosity move along inclined lines in the (k_1, k_3) space and so in the present exploration $|k_3 - k_3^{iso}|$ is *not* the distance from the FP. The relation between δk_3 and $|k_3 - k_3^{iso}|$ is however of immediate determination: in fact, from equation (5) $k_3 = k_3^{iso} + \sqrt{2/3}(k_1 - k_1^{iso})$, and from the assumption that the parent isotropic models are placed on the FP one obtains $\delta k_3 = (1 - 0.15\sqrt{3/2})|k_3 - k_3^{iso}| \simeq 0.816|k_3 - k_3^{iso}|$.

3.1 One-component models

In order to answer to the questions outlined above, we performed a set of 21 simulations of one-component γ models with $\gamma = (0, 1, 2)$, evaluating numerically for each of the three families the critical value for stability s_{as}. We recall here that in our simulations the onset of instability is just the result of numerical noise produced by discreteness effects in the initial conditions, and that, at most, the simulations are interrupted after $100T_{dyn}$. As a rule, in order to determine if a given model is unstable, we found it useful to check its departures from spherical symmetry by monitoring the evolution of its intrinsic axis ratios c/a and b/a (where a, b and c are the longest, intermediate and shortest axis of its inertia ellipsoid associated with 'bona fide' bound particles, see the Appendix): we found that numerical uncertainties (owing to the finite number of particles) of these ratios never exceed 5 per cent. According to this choice we define as *unstable* the models for which the minimum c/a over $100T_{dyn}$ is smaller than a fiducial threshold value, 0.95 (the horizontal dashed line in Fig. 1). Also this value has been obtained by analysing the fluctuations – arising from the finite number of particles – of c/a shown by the numerical realizations of the isotropic (stable) parent γ models. As expected, we found that an exact determination of s_{as} for a given density profile is not straightforward: in fact, while for strongly anisotropic initial conditions the onset of instability is apparent and the numerical models settle down into a final equilibrium configuration in a few dynamical times, for nearly stable initial conditions the instability can be characterized by very slow growth rates and its

effects become evident even after $30T_{dyn}$ (see also Bertin et al. 1994).

The result of the simulations are summarized in Fig. 1, where we plot for all models the final value of the axis ratio, $(c/a)_{fin}$, as a function of ξ (left panel) and r_a/r_M (right panel) of the initial conditions (we recall here that r_M is the spatial half-mass radius). A first result is that for one-component γ models (full symbols) the ξ critical value is in the range $1.6 \lesssim \xi_s \lesssim 1.8$: for $\xi \lesssim 1.6$ all models were found stable up to $100\ T_{dyn}$, while for $\xi \gtrsim 1.8$ all models present clear evolution on time-scales shorter than $30\ T_{dyn}$. This range for ξ_s is compatible with the value 1.7, reported by FP84 and used in CL97, and with the results of Bertin et al. (1994), who estimated $\xi_s \simeq 1.58$ for the family of 'f_∞ models'; Meza & Zamorano (1997) found instead a higher threshold value for stability ($\xi_s \simeq 2.3$). When expressed in terms of r_a/r_M the critical value for stability is found in the range $0.6 \lesssim (r_a/r_M)_s \lesssim 0.8$. Finally, the stability limits expressed in terms of the (dimensionless) critical anisotropy radius (the quantity of direct interest in this work) are given by $s_{as} = (3.0, 1.8, 0.6)$ for $\gamma = (0, 1, 2)$ models, respectively; for comparison the critical anisotropy radius for consistency is $s_{ac} = (0.5, 0.2, 0.0;$ Ciotti 1999).

For what concerns the internal structure of the end-products of unstable initial conditions we found (in accordance with previous results, see e.g. Merritt & Aguilar 1985, Stiavelli & Sparke 1991) that they are in general prolate systems, with axis ratios in the range $0.3 \lesssim (c/a)_{fin} \lesssim 1$, consistent with the ellipticities of the observed galaxies. Only the most anisotropic models, near the consistency limit ($s_a \simeq s_{ac}$), form a triaxial bar. From Fig. 1 it is apparent that
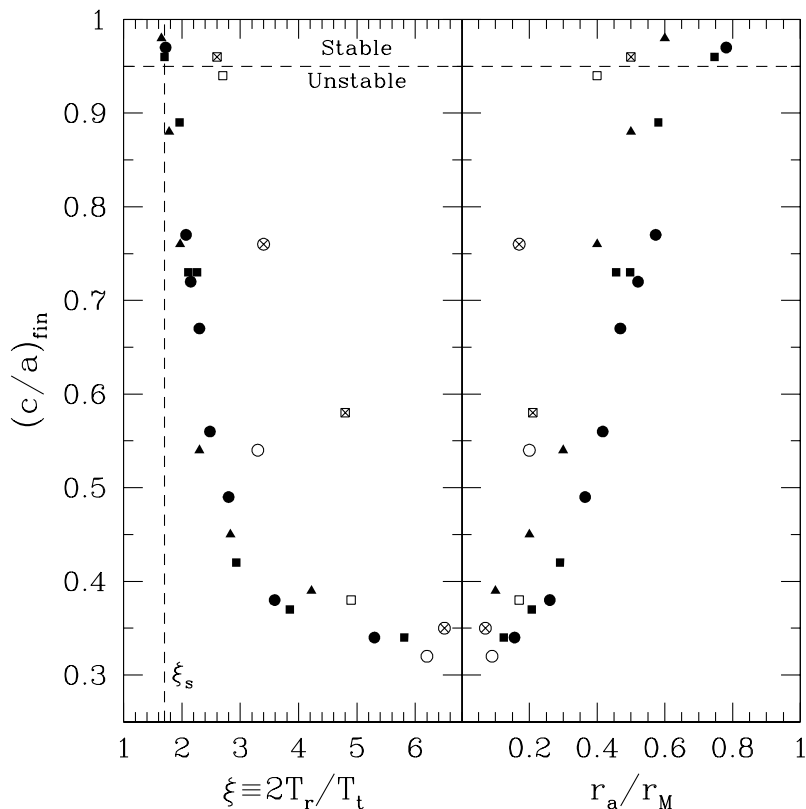

Figure 1. Left: final axis ratio $(c/a)_{fin}$ versus the stability parameter $\xi \equiv 2T_r/T_t$ of initial conditions, for all the computed models. One-component models are represented by full symbols ($\gamma = 0$, circles; $\gamma = 1$, squares; $\gamma = 2$, triangles). Two-component (1,1) models are represented by empty symbols: squares correspond to concentrated haloes ($\beta = 0.5$), circles to diffuse haloes ($\beta = 2$). Crosses indicate models with massive haloes ($\mu = 3$). Right: final axis ratio $(c/a)_{fin}$ versus r_a/r_M for the same models shown in left panel. The vertical dashed line is located at $\xi_s = 1.7$ (FP84). Models above the horizontal dashed line are stable (see the text for a discussion).

$(c/a)_{\rm fin}$ is strongly anti-correlated with ξ (and so correlated with $r_{\rm a}/r_{\rm M}$), and this in a way essentially independent of the value of γ; a similar decrease of $(c/a)_{\rm fin}$ with $s_{\rm a}$ was also found in the numerical simulations of Meza & Zamorano (1997).

In order to compare the end-products of unstable models better with real galaxies, we also fitted their projected mass density profiles with the widely used Sersic (1968) $R^{1/m}$ law:

$$I(R) = I_0 \exp\left[-b(m)\left(\frac{R}{R_{\rm e}}\right)^{1/m}\right],\qquad(22)$$

where $b(m) \sim 2m - 1/3 + 4/405m$ (Ciotti & Bertin 1999). In Fig. 2 we plot the Sersic best-fitting parameter m as a function of ξ for a small, but representative, set of models. As for real galaxies, we found a significant dependence of m on the adopted radial range over which the fit is performed, while the value of m is not very sensitive to the specific fitting method adopted (see e.g. Bertin, Ciotti & Del Principe 2002). For example, in the radial range $0.1 \lesssim R/\langle R\rangle_{\rm e} \lesssim 4$ we found $1 \lesssim m \lesssim 5$, with average residuals between the data and the fits $\langle\Delta\mu\rangle \simeq 0.02\text{–}0.14\,{\rm mag\,arcsec}^{-2}$. Clearly, the fitted quantities m and $\langle R\rangle_{\rm e}$ depend on the relative orientation of the line of sight and of the end-products of the simulations: with the vertical bars in Fig. 2 we indicate the range of values spanned by m when projecting the final states along the short and long axis of their inertia ellipsoids. As an example of the fit for a specific model, in Fig. 3 we show the data relative to the initial conditions of an unstable $\gamma = 1$ model, and to the two projections of its end-products.

Having determined for each family of galaxy models the critical anisotropy radius, we can now proceed to check how distant from the FP stable models can be placed, and where the end-products of unstable initial conditions are found. Of course, in this second case the coordinates in k space depend on the line-of-sight orientation with respect to the density distribution of the end-products, and the dependence is expected to be stronger for smaller values of $(c/a)_{\rm fin}$: to any unstable initial condition corresponds, in the k space, a *set* of points. Owing to the fact pointed out above that the properties of the models investigated here do not depend on the specific position of the parent galaxy on the FP, in Fig. 4 we plot the obtained results in a coordinate system that reflects this property, and allows for an immediate visualization of the most important consequences derived from the simulations; in Fig. 5 the behaviour of a representative set of models is shown in the standard (k_1, k_2, k_3) space. On the horizontal axis of Fig. 4 we plot the displacement of the anisotropic initial conditions, measured by their $k_3^{\rm i}$, with respect to the isotropic parent galaxy, placed at $k_3^{\rm iso}$: as a consequence, initial conditions with larger $|k_3^{\rm i} - k_3^{\rm iso}|$ are characterized by larger amounts of radial orbital anisotropy. As already discussed in the Introduction, these initial conditions are placed in the (k_1, k_3) space along the lines given by equation (5). For example, in the upper panel of Fig. 5 the initial conditions A_1, B_1, and C_1 correspond to the isotropic parent galaxies placed at points A, B, and C (by assuming $\Upsilon_* = 5$ and determining $L_{\rm B}$ from equation 7), while in the lower panel the same parent galaxies and initial conditions are shown in the (k_1, k_2) space, connected by dotted lines.
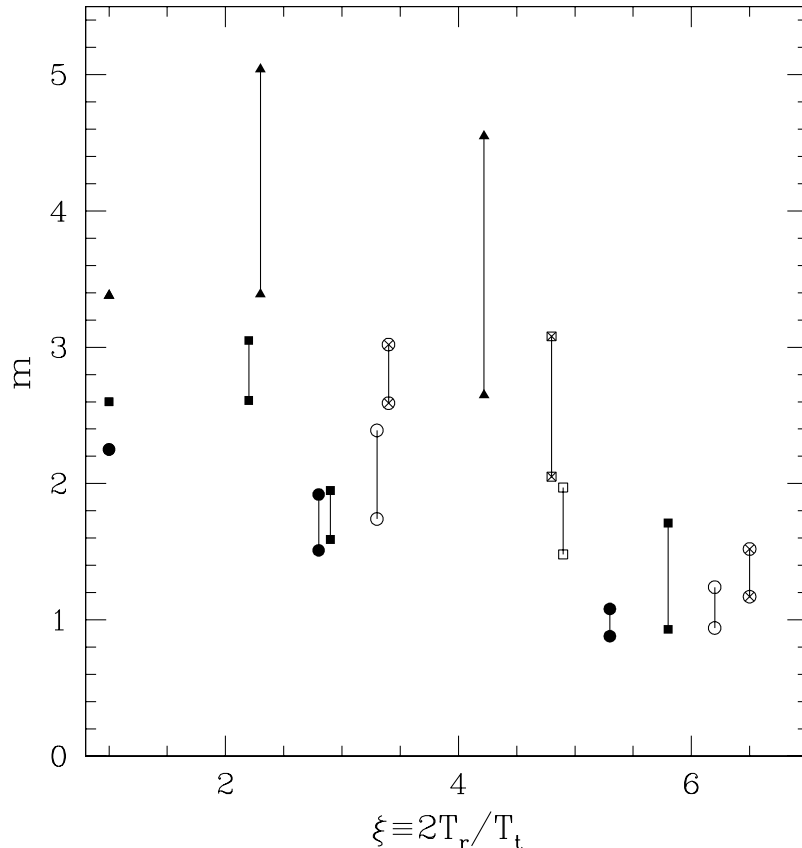

Figure 2. Sersic best-fitting parameter m versus stability parameter ξ for a subset of the computed models. Symbols are the same as in Fig. 1. The three points at $\xi = 1$ give the value of m for the isotropic (stable and spherically symmetric) parent galaxies, while vertical bars show the maximum and minimum m for each model owing to the relative orientation of the end-product and the line of sight.
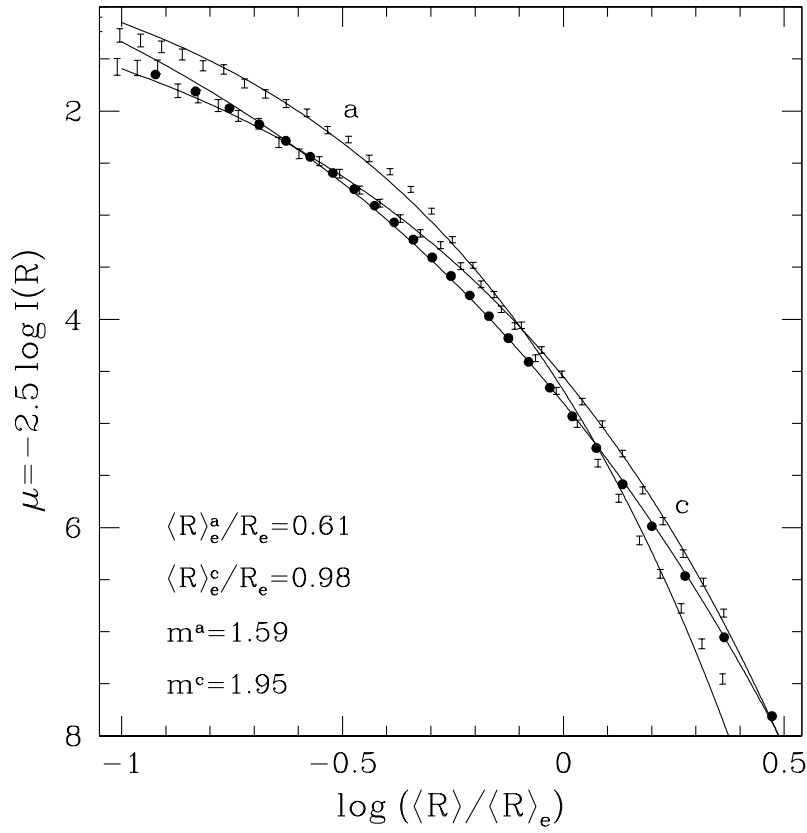
Figure 3. Circularized surface brightness profiles (vertical bars) of the end-product of the unstable one-component $\gamma = 1$ model with $s_a = 0.7$. R_e is the effective radius of the (spherically symmetric) initial condition (solid dots), while $\langle R \rangle_e \equiv \sqrt{a_e b_e}$ is the circularized effective radius. Solid lines represent the best-fitting Sersic models of the end-product projections along its inertia ellipsoid minor (c) and major (a) axis.
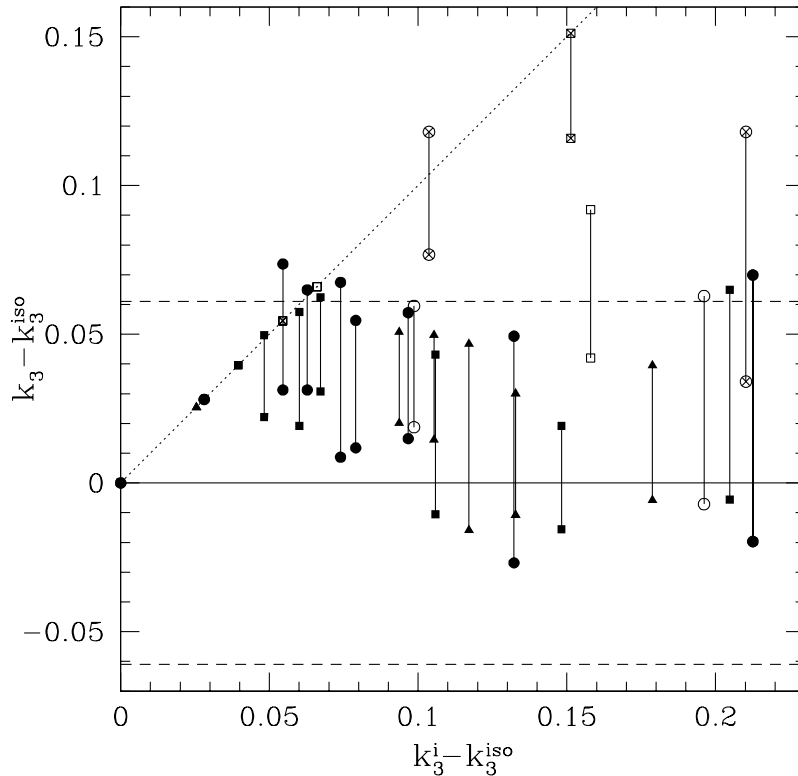

Figure 4. Final versus initial k_3 for all galaxy models, measured with respect to k_3^{iso}, the k_3 coordinate of their isotropic parent galaxy. The horizontal dashed lines correspond to $\delta(k_3) = \sigma(k_3)$, while the dotted line $k_3 = k_3^i$ is the locus of the initial conditions and of the stable models. Symbols are the same as in Fig. 1. See the text for an explanation.

On the vertical axis of Fig. 4 we plot the quantity $k_3 - k_3^{\text{iso}}$ corresponding to the end-product of each explored initial condition: if $k_3 = k_3^{\text{iso}}$ then the model has 'fallen back' on the FP. We also recall here that $\delta k_3 \simeq 0.816 |k_3 - k_3^{\text{iso}}|$: in Fig. 4 the two horizontal dashed lines correspond to the FP thickness $\sigma(k_3)/0.816 \simeq 0.0613$, and so points inside this strip represent models consistent with the observed thickness of the FP. Finally, as an obvious consequence of the choice of the coordinate axes in

Fig. 4, note that all the *initial conditions* (as for example models A_1, B_1, and C_1) are located at $t = 0$ on the dotted line (with slope equal to 1). This means that this line is also the locus of *stable* models, while all the parent galaxies (as for example models A, B, and C of Fig. 5) lie at the point (0,0). A few stable anisotropic models may in fact be seen, as single solid points, on this line at low anisotropy values.

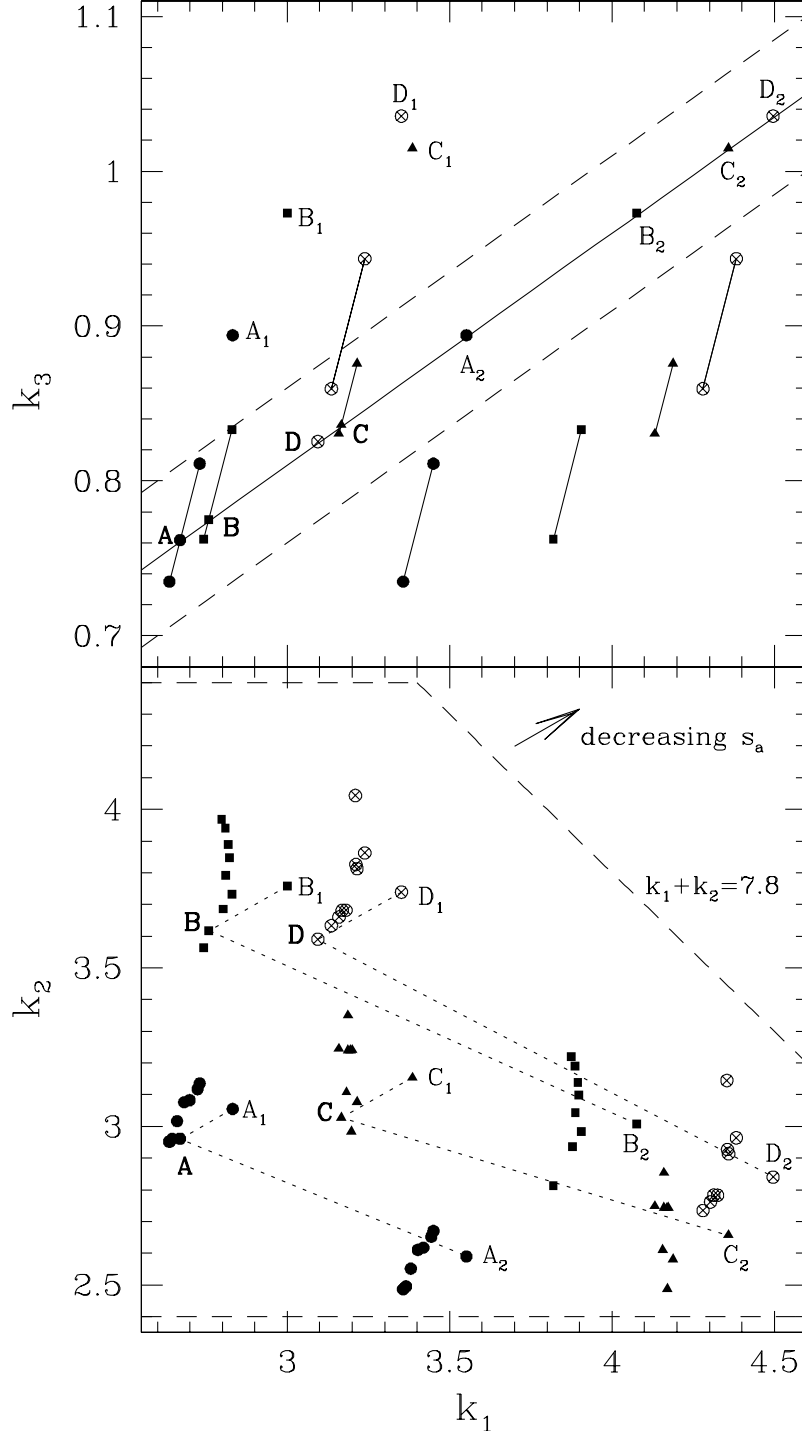By increasing the amount of radial anisotropy the initial

Figure 5. Top: k_3 versus k_1 for a representative set of the one- and two-component models shown in Figs 3 and 4: symbols are the same. The solid line represents the FP relation (equation 4) with its observed dispersion (dashed lines). The stellar mass-to-light ratio is fixed at $Y_* = 5$ and $Y_* = 2.7$, for one- and two-component models, respectively. Bottom: k_2 versus k_1 for the same models plotted in the upper panel. The dashed lines define the region, as given by BBF, where real galaxies are found. The arrow shows the direction followed by initial conditions with increasing radial anisotropy.

conditions move along the dotted line, and when they reach the critical value of the anisotropy radius they become unstable and rearrange their density profile and internal dynamics in a new, stable configuration. As we have seen, these end-products are strongly asymmetric, and so their representative points span a range of values as a function of the line-of-sight orientation. In Fig. 4 the vertical lines show the importance of this projection effect: note that, in general, the length of these segments is considerably smaller than the FP thickness.

The first result that can be obtained by inspection of Fig. 4 is the fact that, for one-component γ models (solid symbols), radial orbit instability becomes effective for initial conditions *inside* the FP thickness, thus providing strong support to the results of CL97 for $R^{1/m}$ models. In contrast, by considering as anisotropy limitation the very basic requirement of model consistency only, it is apparent from Fig. 4 that physically acceptable initial conditions could be placed at a distance from the FP substantially larger than $\sigma(k_3)$, up to $\delta k_3 \simeq 2 - 3\sigma(k_3)$, the well-known problem motivating this work. Models A_1, B_1, and C_1 in Fig. 5 are just three examples of such models. The second result is that all one-component, radially unstable models fall back on the FP: in other words, *not only is the FP thickness nicely related to stability, but the FP itself acts as an 'attractor' for the end-products of radially unstable systems when their parent galaxies lie on it.*

The same results can be illustrated in a more direct way by using Fig. 5, where we plot the positions of the end-products of unstable models in the k space. As described above, to each final configuration derived from unstable initial conditions corresponds a set of points, depending on their relative orientation with respect to the observer's line of sight. Owing to the fact that the total luminosity of each model is obviously conserved by projection, these sets in the (k_1, k_3) space are actually *segments* of the straight line given by equation (5), as shown by Fig. 5 where the end-products of the initial conditions A_1, B_1, and C_1 can be immediately recognized. In contrast, in the (k_1, k_2) plane the end-products are distributed, as a consequence of projection along different angles, on two-dimensional regions. This is a result of the fact that no one-to-one relation similar to equation (5) exists between k_1 and k_2, because the value of $\langle R \rangle_e$ also enters explicitly $[k_2 = \log(\Upsilon_* L_B^3 / K_V \langle R \rangle_e^6)/\sqrt{6} + const]$. For this reason for each end-product we plot several positions obtained with random viewing angles. Note however that the displacement in the (k_1, k_2) space occurs mainly along the k_2 coordinate, and this is caused by the steepening of the profile (Fig. 2), i.e. by the increase in $\langle I \rangle_e$. *In any case, the models remain well inside the populated zone of the (k_1, k_2) plane.*

3.2 Two-component models

We now present the results of the numerical simulations (8) of two-component $(1,1)$ galaxy models. In fact, although indications exist that the *onset* of radial orbital anisotropy is not strongly affected by the presence of a massive DM halo (see e.g. Stiavelli & Sparke 1991; Ciotti 1996), in principle its *presence* could significantly modify the structural and dynamical properties of the end-products of unstable initial conditions, and so alter the findings obtained for one-component models described in Section 3.1.

Unfortunately, owing to the dimension of the parameter space, we are not in the position to determine, as for one-component models, even a fiducial threshold for stability, and so we limit our study to the behaviour of some representative models. In particular, we consider the following cases: $\mu = 1$ ('light' halo), $\mu = 3$

('massive' halo), $\beta = 0.5$ ('concentrated' halo) and $\beta = 2$ ('diffuse' halo), where for each of the four possible combinations we fix the anisotropy radius to $s_a = 0.3$ and $s_a = 0.7$, two values corresponding to strongly unstable one-component $\gamma = 1$ models. In all the simulations we use *live* DM haloes, and in order to have equal mass particles for 'stars' and 'dark matter' we adopt $N_h = 98\,304$ and $N_* = 32\,768$ for $\mu = 3$, and $N_h = N_* = 65\,536$ for $\mu = 1$.

In analogy with the one-component case, the quantities T_r and T_t, entering the definition of $\xi = 2T_r/T_t$, are now the radial and the tangential component of the *total* (stellar and halo) kinetic energy tensor, respectively. This choice seems the natural one in the case of a live DM halo, when from a dynamical point of view the galaxy should be considered as a whole; but certainly other choices (for example, by using in the ξ definition the kinetic energies of the stellar component only) could be equally well motivated. Clearly, the determination of the observational properties of the end-products is based on the analysis of their stellar component only.

As can be seen from Fig. 1, where the ellipticity of the stellar component of $(1,1)$ models is represented by empty symbols, the basic trend of $(c/a)_{fin}$ with ξ is similar to that of one-component models: the end-products are mostly prolate systems, with axis ratio $(c/a)_{fin}$ in the same range of that of the one-component models. In general, however, when considering one- and two-component initial conditions with the same ξ, the final *stellar* distribution remains more spherical in the cases with DM than in the one-component cases. Moreover, models with massive DM haloes (empty symbols with crosses in Figs 1, 2, 4 and 5) remain more spherical than the corresponding models with light haloes and (approximately) the same ξ. This means that for the explored two-component models, at variance with the one-component cases, the parameter ξ *is not* well correlated with the final axis ratio. As can be seen from Fig. 2, the best-fitting parameter m of the projected stellar distribution of the end-products of $(1,1)$ unstable models remains limited to values $m \lesssim 3$, the same range covered by one-component $\gamma = 1$ models. We also found that the final shape of the DM haloes remains nearly spherical, with $0.88 \lesssim (c/a)_{fin} \lesssim 1$.

The observational properties of the end-products of the two-component models are illustrated in Figs 4 and 5 where a comparison with the one-component models can be easily made. In particular, as in the one-component case, we found that the FP thickness still nicely separates stable from unstable models, independently of the amount and distribution of DM. However, the final position in the k space of the end-products depends on the amount of DM: as expected, two-component models with a light halo (quite independently of its concentration) are very similar to one-component models, while models with massive DM haloes are quite different. In particular from Fig. 4 it is apparent that massive haloes prevent the models from falling back on the FP and this effect is stronger for more concentrated haloes. This is shown in Fig. 5 (upper panel) by the final state of model D_1, an initial condition obtained from the parent galaxy D, and characterized by a diffuse, massive DM halo. The positions of this end-product in the (k_1, k_2) plane are instead remarkably similar to those of the one-component models, and the same comments apply. Again, the scatter associated with projection effects is smaller than the total thickness of the FP.

4 ORBITAL ANISOTROPY AND THE FP TILT

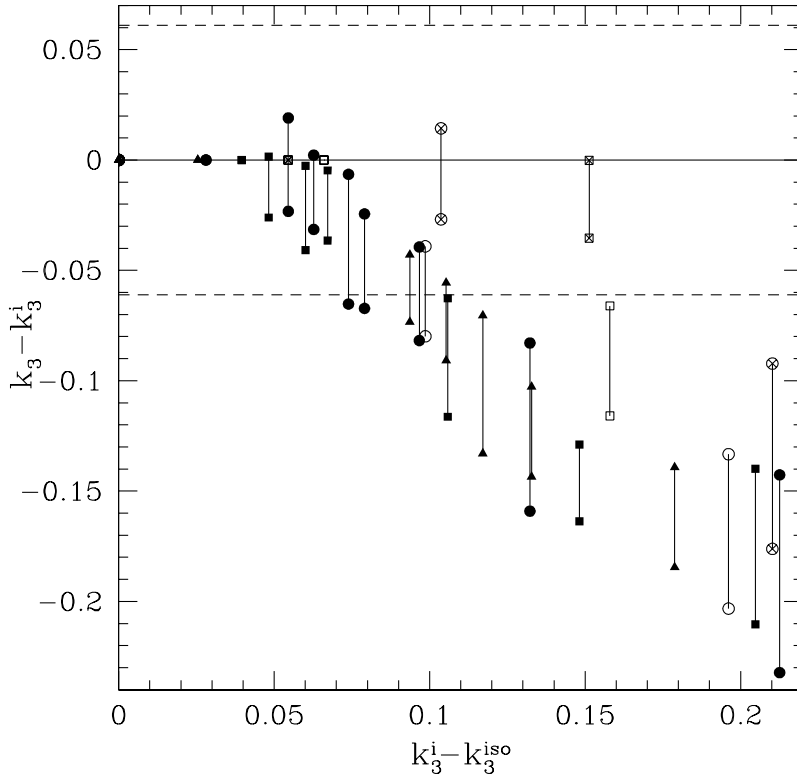As discussed in the Introduction, a question frequently addressed in

Figure 6. End-products of initial conditions placed on the FP at $k_3^i - k_3^{iso}$, where k_3^{iso} is the coordinate of their isotropic parent galaxy. The dashed lines correspond to $\delta k_3 = \sigma(k_3)$. Note that the abscissae range is significantly smaller than the actual range spanned by BBF galaxies, $\Delta k_3 \simeq 0.3$. Symbols are the same as in Fig. 4.

the literature is whether the so-called FP tilt can be caused by some kind of structural and/or dynamical 'non-homology', i.e. a systematic variation from low to high luminosities of the structural and/or dynamical properties of the galaxies. From an observational point of view, this problem is still in general unsettled (see e.g. Caon, Capaccioli & D'Onofrio 1993; Graham & Colless 1997; Gerhard et al. 2001; Bertin et al. 2002 and references therein) and so here we try to gain some hints on its solution by using the results of the numerical simulations described in Section 3. In particular we investigate whether relation (7) can be satisfied, in the whole observed luminosity range ($0.2 \lesssim L_B \lesssim 40$ in the BBF sample), by a systematic variation of K_V induced by an appropriate underlying correlation $s_a = s_a(L_B)$, while maintaining fixed the model structure and Υ_*. In practice, the isotropic parent model of each family is placed on the FP by selecting its L_B and Υ_*; then, by increasing its anisotropy and luminosity, the family of initial conditions is generated. Note that, at variance with the exploration described in Section 3, in this case all the initial conditions are placed by construction on the FP, as can be seen from Fig. 5 (upper panel) where initial conditions A_2, B_2, C_2 and D_2 are generated by the parent galaxies A, B, C and D.

As in the case of Section 3, we found it useful to represent the result of the simulations in a coordinate system slightly different from the usual k space. In the abscissae axis of Fig. 6 we plot the quantity $k_3^i - k_3^{iso}$ that measures how much a given initial condition is displaced on the FP from its parent isotropic model, while in the ordinate axis we plot the quantity $k_3 - k_3^i$ of the corresponding end-product. As a consequence all the parent isotropic models are placed at the origin, and the FP is represented by the solid line $k_3 = k_3^i$: this line is also the line of stable initial conditions, while the two horizontal dashed lines represent the FP thickness. By

using an argument similar to that used in the case of Fig. 4, we now obtain $\delta k_3 \simeq 0.816|k_3 - k_3^i|$ and the end-products of unstable initial conditions are vertical segments owing to projection effects.

4.1 One-component models

For each family of γ models we fixed a constant value of Υ_* such that the isotropic model, with a suitable assigned L_B, lies at the faint end of the FP ($k_1 \simeq 2.6$, $k_3 \simeq 0.75$). Then we placed the anisotropic initial conditions on the FP by choosing L_B, according to equation (7), as a function of $K_V = K_V(\gamma, s_a)$, in order to reproduce the tilt of the FP.

The inspection of Fig. 6 reveals that it is not possible to reproduce the FP tilt over the whole observed range ($\Delta k_1 \simeq 2$ and $\Delta k_3 \simeq 0.3$ in the BBF sample) by using stable models only. In fact, independently of the value of γ, the variations of K_V for $s_a \gtrsim s_{as}$ correspond to $\Delta k_3 \lesssim 0.04$, much smaller than the observed interval. If we consider also unstable (but consistent) systems, we can use a wider range of $K_V(\gamma, s_a)$ (cf. Table 1). In this case it is possible to reproduce the FP tilt over a much larger interval, $\Delta k_3 \simeq 0.2$, which is, however, still significantly smaller than the observed one: even if consistency limitations only are taken into account, *the FP tilt cannot be explained as an effect of a systematic increase of radial anisotropy in one-component models, under the assumption of structural homology* (see also CLR96 and CL97).

What happens to the end-products of unstable initial conditions is shown in Fig. 6: in general they fall well outside the FP thickness, and the departure is larger for larger distance from the parent galaxy: they always fall out of $\sigma(k_3)$ for $k_3^i - k_3^{iso} \simeq 0.1$: this implies that, limiting ourselves to end-products of unstable

initial conditions that remain *inside* the FP thickness, the maximum amount of the FP tilt that can be explained by pure anisotropy is $k_3^i - k_3^{iso} \lesssim 0.1$. Of course, a *larger* part of the FP tilt could be covered by considering parent galaxies with *tangentially anisotropic* velocity dispersion tensor (as observed in real, low luminosity ellipticals).

The results presented can also be seen, for a few representative cases, in the upper panel of Fig. 5, where the position of the end-products of models A_2, B_2, C_2, D_2 is represented by the straight-line segments. As in the case discussed in Section 3, the end-products remain well inside the region populated by real galaxies in the (k_1, k_2) plane.

Finally we qualitatively explore an interesting related problem (which however is not the argument of our paper), i.e. whether the FP tilt can be reproduced over the whole observed range in luminosity, for fixed Υ_*, in the case in which the requirement of perfect structural homology is relaxed. In practice we determined Υ_* so that the parent isotropic $\gamma = 0$ model (to which the maximum value of K_V corresponds) is placed at the faint end of the FP ($L_B = 0.2$, $\Upsilon_* = 5$). With the same value of Υ_*, the $\gamma = 1$ and $\gamma = 2$ parent galaxies are then placed on the FP, and their positions are characterized by larger L_B (and so k_1), owing to the corresponding decrease of K_V (see first column in Table 1). In this approach, the FP tilt can be reproduced over almost all the observed range by using models compatible with *consistency*. However, even in this *mixed* structural and dynamical non-homology approach, if one limits oneself to *stable* models only, the maximum available range is reduced to $\Delta k_3 \simeq 0.16$, approximately half of the required k_3 variation.

4.2 Two-component models

In analogy with the one-component case, for each family of $(1,1)$ models, given μ, β (the same as for the models presented in Section 3.2) and Υ_*, we placed the parent isotropic model at the faint end of the FP and we derived L_B of the initial conditions according to equation (7), as a function of $K_V = K_V(\mu, \beta, s_a)$. As already discussed in Section 3.2, for each family of $(1,1)$ models we study only two values of the anisotropy radius, $s_a = 0.3$ and $s_a = 0.7$. We found that for each family these initial conditions, under the only requirement of consistency ($s_a \gtrsim s_{ac}$), span a range $\Delta k_3 \lesssim 0.2$, smaller than the observed one (see Fig. 6). The main difference with respect to the one-component case is that in the (k_1, k_3) space the end-products of the unstable $(1,1)$ models move less than the one-component models with similar initial δk_3 and only the most anisotropic systems fall outside the FP thickness. An example of these systems is model D_2, whose behaviour in the (k_1, k_3) and (k_1, k_2) planes, clearly represented in the upper and lower panel of Fig. 5 respectively, is similar to that of one-component models (A_2, B_2, C_2). Again we found that the DM halo concentration is an important quantity, strictly related to the displacement of the end-product with respect to the initial conditions.

These findings suggest that *even in the two-component case under the assumption of perfect structural homology and constant mass-to-light ratio, the FP tilt cannot be explained as a consequence of a systematic increase of radial orbital anisotropy.*

5 DISCUSSION AND CONCLUSIONS

With the aid of numerical simulations of one and two-component galaxy models we explored the constraints imposed by the observed thickness and tilt of the FP on the amount and distribution of radial orbital anisotropy in elliptical galaxies. The main results are summarized below.

(i) Remarkably, all the explored models (both one and two-component, and quite independently of the density profile) are found to be unstable when their orbital radial anisotropy is high enough to place them outside the observed FP thickness (under the assumption that their isotropic parent models lie on the FP). In contrast, all stable models lie inside the FP thickness.

(ii) The end-products of one-component unstable models initially placed outside the FP fall back inside the FP: in other words, the larger the initial displacement from the FP, the stronger the reassessment of the model structure and dynamics. The behaviour of two-component models is more varied, owing to the fact that the properties of their end-products are significantly affected by the amount of mass and the distribution of the DM halo. In particular, the end-products of models with massive (either concentrated or diffuse) DM haloes remain outside the FP thickness, while models with light haloes behave essentially like one-component models.

(iii) Since the end-products of the unstable initial conditions are not spherically symmetric, their positions on the (k_1, k_3) plane depend on their relative orientation with respect to the line-of-sight direction. However, the scatter arising from projection effects is in general smaller than the observed thickness of the FP, both for one-and two-component models.

(iv) We found that it is impossible to reproduce the whole FP tilt with radially anisotropic but stable (one and two-component) models under the assumption of constant Υ_* and structural homology. In other words, under these assumptions, luminous galaxies would be radially unstable well before the bright end of the FP.

(v) At variance with what happens to the end-products of unstable models initially placed outside the FP thickness (but exactly for the same reasons), the end-products of unstable models with initial conditions on the FP fall well outside the FP itself.

Our results lead to some speculation on the formation mechanism and evolutionary scenarios of elliptical galaxies. First, if the (unknown) formation mechanism produces galaxies with various degrees of internal radial orbital anisotropy, of which the isotropic ones constitute the 'backbone' of the observed FP, then the most anisotropic systems would be radially unstable and would evolve into final states lying on the FP. Then no 'ad hoc' fine tuning would be required on the amount of radial anisotropy of ellipticals at the moment of their formation. In addition, our results concerning the FP tilt could give some indications about the importance of dissipationless merging in the history of the assembly of elliptical galaxies. In fact, if Es form by hierarchical *dissipationless* merging, then the very existence of the FP necessarily implies structural or dynamical non-homology of the merging end-products. The possibility that we explored in this work is that of a substantial dynamical non-homology as a function of galaxy luminosity. Our simulations show that this is not a viable possibility to reproduce the FP tilt: in this scenario the FP would be destroyed by merging. However, it should be clear that we cannot rule out the possibility that merging produces a combination of structural and dynamical effects that conspire to maintain galaxies on the FP. For this reason we are now exploring this problem, with the aid of one and two-component galaxy merging simulations.

All our results on the FP thickness and tilt seem to point toward a significant dynamical homology in real galaxies, and dynamical

homology in luminous Es has been recently determined by some authors (Gerhard et al. 2001); we note also that an independent observational support for dynamical homology is given by the very evidence of the $M_{BH}-\sigma_0$ relation, which relates a dynamical independent quantity (M_{BH}) with a quantity strongly dependent on anisotropy (σ_0). The fact that the scatter of the $M_{BH}-\sigma_0$ is very small means that elliptical galaxies are basically dynamically homologous systems.

REFERENCES

Athanassoula E., Fady E., Lambert J. C., Bosma A., 2000, MNRAS, 314, 475
Barnes J. E., Hut P., 1986, Nat, 324, 446
Barnes J. E., Hut P., 1989, ApJS, 70, 389
Bender R., 1988, A&A, 193, 7
Bender R., Burstein D., Faber S. M., 1992, ApJ, 399, 462 (BBF)
Bender R., Burstein D., Faber S. M., 1993, ApJ, 411, 153
Bender R., Saglia R. P., Ziegler B., Belloni P., Greggio L., Hopp U., Bruzual G., 1998, ApJ, 493, 529
Bertin G., Stiavelli M., 1989, ApJ, 338, 723
Bertin G., Pegoraro F., Rubini F., Vesperini E., 1994, ApJ, 434, 94
Bertin G., Ciotti L., Del Principe M., 2002, A&A, in press
Binney J. J., Tremaine S., 1987, Galactic Dynamics. Princeton Univ. Press, Princeton
Bower R. G., Lucey J. R., Ellis R. S., 1992, MNRAS, 254, 601
Caon N., Capaccioli M., D'Onofrio M., 1993, MNRAS, 265, 1013
Capelato H. V., de Carvalho R. R., Carlberg R. G., 1995, ApJ, 451, 525
Carollo C. M., de Zeeuw P. T., van der Marel R. P., 1995, MNRAS, 276, 1131
Ciotti L., 1996, ApJ, 471, 68
Ciotti L., 1997, in da Costa L., Renzini A., eds, 3rd ESO-VLT Workshop – Galaxy Scaling Relations: Origins, Evolution and Applications. Kluwer, Dordrecht
Ciotti L., 1994, Celest. Mech. Dyn. Astron., 60, 401
Ciotti L., 1999, ApJ, 520, 574
Ciotti L., Bertin G., 1999, A&A, 352, 447
Ciotti L., Lanzoni B., 1997, A&A, 321, 724 (CL97)
Ciotti L., van Albada T. S., 2001, ApJ, 552, L13
Ciotti L., Lanzoni B., Renzini A., 1996, MNRAS, 282, 1 (CLR96)
Dehnen W., 1993, MNRAS, 265, 250
Dehnen W., 2001, MNRAS, 324, 273
de Vaucouleur G., 1948, Ann. d'Astrophys., 11, 247
de Zeeuw T., Franx M., 1991, ARA&A, 29, 239
Djorgovsky M., Davis S., 1987, ApJ, 313, 59
Dressler A., Faber S. M., Burstein D., Davies R. L., Lynden-Bell D., Terlevich R. J., Wegner G., 1987, ApJ, 313, 37
Faber S. M., Jackson R. E., 1976, ApJ, 204, 668
Ferrarese L., Merritt D., 2000, ApJ, 539, L9
Fridman A. M., Polyachenko V. L., 1984, Physics of Gravitating Systems. Springer, New York (FP84)
Gebhardt K. et al., 2000, ApJ, 539, L13
Gerhard O., Kronawitter A., Saglia R. P., Bender R., 2001, AJ, 121, 1936
Graham A., Colless M., 1997, MNRAS, 287, 221
Hernquist L., 1987, ApJS, 64, 715
Hernquist L., 1990, ApJ, 356, 359
Jaffe W., 1983, MNRAS, 202, 995

Jørgensen I., Franx M., Kjærgaard P., 1996, MNRAS, 280, 167
Merritt D., 1985, AJ, 90, 102
Merritt D., 1996, AJ, 111, 2462
Merritt D., Aguilar L. A., 1985, MNRAS, 217, 787
Meza A., Zamorano N., 1997, AJ, 490, 136
Naab T., Burkert A., Hernquist L., 1999, ApJ, 523, L133
Navarro J. F., Frenk C. S., White S. D. M., 1996, ApJ, 462, 563
Osipkov L. P., 1979, Sov. Astron. Lett., 5, 42
Pahre M. A., Djorgovski S. G., de Carvalho R. R., 1998, AJ, 116, 1591
Renzini A., Ciotti L., 1993, ApJ, 416, L49
Saha P., 1991, MNRAS, 148, 494
Saha P., 1992, MNRAS, 254, 132
Sersic J. L., 1968, Atlas de galaxias australes. Observatorio Astronomico, Cordoba
Springel V., Yoshida N., White S. D. M., 2001, New Astron., 6, 79
Stiavelli M., Sparke L. S., 1991, ApJ, 382, 466
Tremaine S., Richstone D. O., Yong-Ik B., Dressler A., Faber S. M., Grillmair C., Kormendy J., Laurer T. R., 1994, AJ, 107, 634
Treu T., Stiavelli M., Casertano S., Mœller P., Bertin G., 1999, MNRAS, 308, 1037
van Dokkum P., Franx M., 1996, MNRAS, 281, 985

APPENDIX A: INTRINSIC AND OBSERVATIONAL PROPERTIES OF THE NUMERICAL MODELS

In this Appendix we summarize the techniques used to derive the intrinsic and projected properties of the end-products of the simulations.

As discussed in Section 3.1, the intrinsic ellipticities associated with the inertia ellipsoids of the end-products of the numerical simulations were used as a measure of their departure from spherical symmetry; thus for each numerical simulation we compute the inertia tensor $I_{ij} = \sum_k x_i^{(k)} x_j^{(k)}$ associated with the density distribution of interest (i.e. stars or halo). Following Meza & Zamorano (1997), the sum is extended over all the particles inside r_{70}, the radius of the sphere centred on the centre of mass of the galaxy and enclosing 70 per cent of the total mass. The inertia tensor is diagonalized and the ratios of the square root of its eigenvalues are used to obtain a first estimate of the ellipticities of the density distribution, according to the standard definition $1 - b_{70}/a_{70}$ and $1 - c_{70}/a_{70}$. The orthogonal matrix corresponding to the diagonalization is also obtained, and the density distribution is rotated accordingly. This procedure is then applied iteratively to the ellipsoid characterized by $a = r_{70}$ and with intermediate and minor axes obtained from the ellipticities computed at each stage, up to convergence at some prescribed accuracy level of the ellipticities. Note that this procedure automatically selects bound particles only: in fact, in all our simulations the fraction of 'escapers' never exceeds 0.02 per cent of the total number of particles.

In order to obtain the 'observational' properties of our synthetic galaxies, we calculate the following projected quantities of their stellar component: the isophotal ellipticity ϵ, the circularized effective radius $\langle R \rangle_e$, the mean effective surface brightness $\langle I \rangle_e$, and the central velocity dispersion σ_0. The line-of-sight direction is fixed by the arbitrary choice of ϑ and φ, the two angles of spherical coordinates, expressed in the reference frame where the inertia ellipsoid is diagonal. We apply to the system the rotation matrix $\mathbf{R} = \mathbf{R}_2(\vartheta)\mathbf{R}_3(\varphi)$, where

$$\mathbf{R}_3(\varphi) = \begin{bmatrix} \cos\varphi & \sin\varphi & 0 \\ -\sin\varphi & \cos\varphi & 0 \\ 0 & 0 & 1 \end{bmatrix}, \tag{A1}$$

$$R_2(\vartheta) = \begin{bmatrix} \cos\vartheta & 0 & -\sin\vartheta \\ 0 & 1 & 0 \\ \sin\vartheta & 0 & \cos\vartheta \end{bmatrix}. \tag{A2}$$

In this coordinate system, the line-of-sight direction coincides with the z axis, while (x, y) is the projection plane. The isophotal axis ratio b/a and the associated ellipticity $\epsilon = 1 - b/a$ in the projection plane are determined by using a two-dimensional version of the iterative scheme described above.

The semi-axes a_e and b_e of the effective isophote are determined under the assumption that the ellipticity of the projected density is constant. Finally, the circularized effective radius is obtained:

$$\langle R \rangle_e = \sqrt{a_e b_e} = a_e \sqrt{1 - \epsilon}. \tag{A3}$$

From the knowledge of $\langle R \rangle_e$, the mean effective surface brightness $\langle I \rangle_e \equiv L_B / 2\pi \langle R \rangle_e^2$ is derived modulo the free parameter $\Upsilon_* = M_*/L_B$.

The 'central' velocity dispersion σ_0 is computed, by restricting ourselves to the central ellipse corresponding to a circularized radius $\langle R \rangle_e/8$. Thus we use

$$\sigma_0 = \sqrt{\frac{1}{N}\sum_{i=1}^{N}(v_{z_i} - \bar{v}_z)^2}, \tag{A4}$$

where N is the number of particles in the projected ellipse of semi-axes $a_e/8$ and $b_e/8$, v_{z_i} is the line-of-sight velocity of the ith particle, and $\bar{v}_z$ is the mean velocity integrated along the line of sight. We find that discreteness effects on the derived values of σ_0 range from 0.5 per cent (for $\gamma = 0$ models) to 0.9 per cent (for $\gamma = 2$ models); moreover, the uncertainties on $\langle R \rangle_e$ and $\langle I \rangle_e$ never exceed 0.7 and 1.4 per cent, respectively. In other words, the numerical error bars on the model measurements are significantly smaller than the observed scatter of the FP itself, and so are not important in the context of the paper.

This paper has been typeset from a TeX/LaTeX file prepared by the author.